Supporting Information: Phase Behavior and Ion Transport in Lithium–Niobium–Tantalum Oxide Alloys

Hengning Chen,[†] Zeyu Deng,[†] Gopalakrishnan Sai Gautam,[‡] Yan Li,[†] and Pieremanuele Canepa[*,¶,§]

[†]*Department of Materials Science and Engineering, National University of Singapore, 9 Engineering Drive 1, 117575, Singapore*

[‡]*Department of Materials Engineering, Indian Institute of Science, 560012 Bangalore, India*

[¶]*Department of Electrical and Computer Engineering, University of Houston, Houston, Texas 77204, USA*

[§]*Texas Center of Superconductivity, University of Houston, Houston, Texas 77204, USA*

E-mail: pcanepa@uh.edu

Contents

1 DFT Calculations and Cluster Expansion Fitting for $LiNb_xTa_{1-x}O_3$ and $Li_3Nb_xTa_{1-x}O_4$ Systems **S-3**

2 M-O Bond Lengths and Volume Changes of DFT-calculated Orderings **S-10**

3 Phonon Calculations for $Li_3Nb_xTa_{1-x}O_4$ ground-state structures **S-13**

4 Computed phase diagram of $LiNb_xTa_{1-x}O_3$ **S-19**

5 Thermodynamic Integration **S-22**

6 Li-ion conductivities of $Li_3Nb_xTa_{1-x}O_4$ from MTP-MD simulations **S-24**

References **S-26**

1 DFT Calculations and Cluster Expansion Fitting for $LiNb_xTa_{1-x}O_3$ and $Li_3Nb_xTa_{1-x}O_4$ Systems

To understand the phase behavior of lithium-niobate-tantalate oxides, we investigated both $Li_3Nb_xTa_{1-x}O_4$ (in the main text) and $LiNb_xTa_{1-x}O_3$ (in the SI) systems. Density functional theory (DFT) calculations of mixed orderings were performed using the Vienna Ab initio Simulation Package (VASP).[S1] We employed projector augmented-wave (PAW) potentials with a kinetic energy cutoff of 520 eV for the plane-wave basis set.[S2] The valence electron configurations used were Li 17Jan2003 ($2s^1$), Nb_pv 08Apr2002 ($4p^6 5s^1 4d^4$), Ta_pv 07Sep2000 ($5p^6 6S^2 5d^3$), and O 08Apr2002 ($2s^2 2p^4$). The kinetic energy cut-off describing the valence electrons was set to 520 eV. The exchange-correlation energy was approximated using the r^2SCAN meta-GGA functional.[S3] The first Brillouin zones of the Li_3NbO_4 ($I\bar{4}3m$) and Li_3TaO_4 (C2/c) conventional cells were integrated using $3 \times 3 \times 3$ and $4 \times 4 \times 2$ Γ-centered k-point meshes, respectively. Density-normalized k-point grids were used for larger supercell models of the same materials. The geometries of intermediate compositions, including the lattice parameters and atomic positions, were fully optimized until the interatomic forces were less than 0.01 eVAA, with an electronic energy convergence criterion of 10^{-5} eV.

For the $LiNb_xTa_{1-x}O_3$ system, we first established orderings between $LiTaO_3$ and $LiNbO_3$, both of which share the same $R3c$ space group, with Nb/Ta occupying the 8f site (Figure S1a). The $LiNb_xTa_{1-x}O_3$ system adopts the same distorted perovskite structure as its isostructural end-members across the entire compositional range, corresponding to the experimental observations.[S4] The positive DFT-calculated mixing energy values of Nb/Ta orderings across the entire composition axis (0∼ 5 meV/f.u. with reference to the end structures) indicate a tendency towards phase separation at 0 K (Figure S1b).

To sample different compositions, a total of 306 Nb/Ta orderings, evaluated on 1×1×1 to 2×2×2 supercell models, were selected for CE fitting (Figure S1b). The effective cluster

interactions (ECIs), depicted in Figure S2b, were determined by minimizing the root mean square error (RMSE) against all DFT energies of configurations ($\sim$ 0.18 meV/f.u.), as well as leave one-out cross-validation (LOOCV) score ($\sim$ 0.19 meV/f.u.). The LOOCV defines the robustness of the CE model.

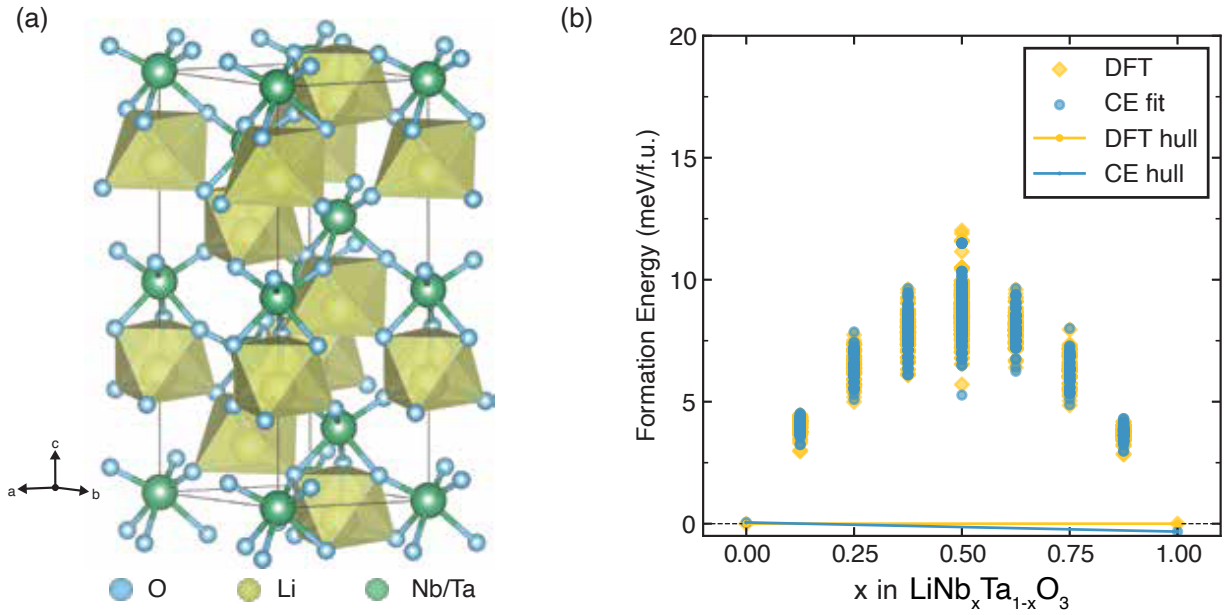

Figure S1: (a) Structural illustration of *R*3*c* $LiMO_3$ (M=Nb, Ta), (b) Configurational mixing energies of $LiNb_xTa_{1-x}O_3$ orderings calculated by DFT (yellow diamonds) and cluster expansion (blue points) fittings. Given that all Nb/Ta orderings exhibit positive mixing energies, the convex hulls are set by the end-member compounds and lie at 0 meV/f.u.

Besides Nb and Ta having similar ionic radii in six-coordinated anion environments, the substitution of Ta with Nb leads to a slight increase in the lattice volume (Figure S3) for the $LiNb_xTa_{1-x}O_3$. Similar findings were reported in existing experimental works of Huband et al.[S4]

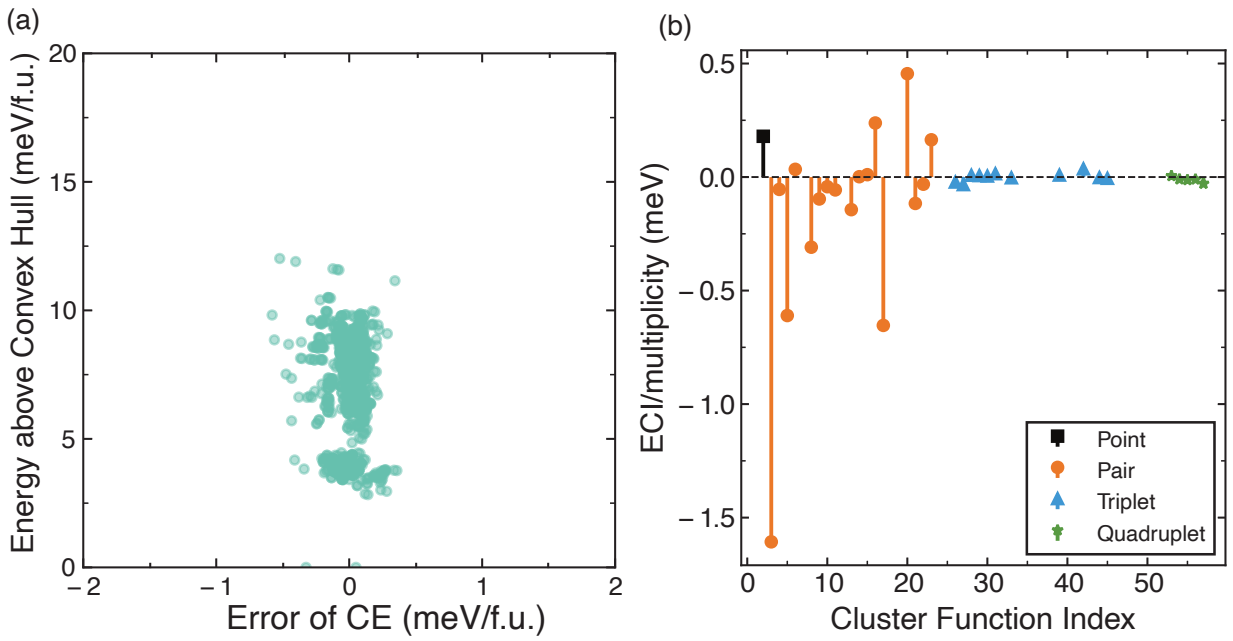

Figure S2: (a) Error of cluster expansion fitting ($E_{\mathrm{CE}} - E_{\mathrm{DFT}}$), (b) ECIs of $\mathrm{LiNb_xTa_{1-x}O_3}$, including point, pairs, triplets, and terminated at quadruplets. The RMS and LOOCV errors are 0.18 meV/f.u. and 0.19 meV/f.u., respectively.

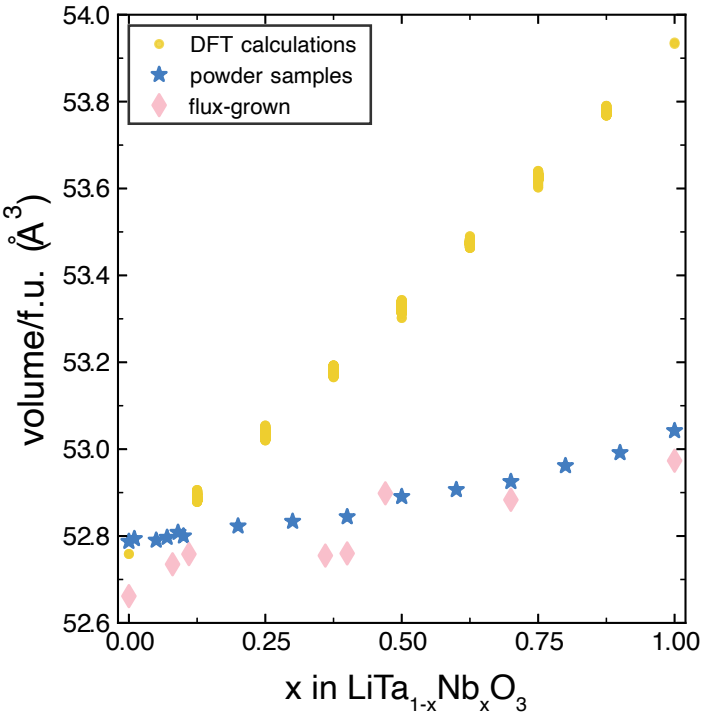

Figure S3: Volumes of $LiNb_xTa_{1-x}O_3$ orderings vary with Nb concentration (x), consistent with experimental trends observed in powder samples and flux-grown samples from Huband et al. [S4]

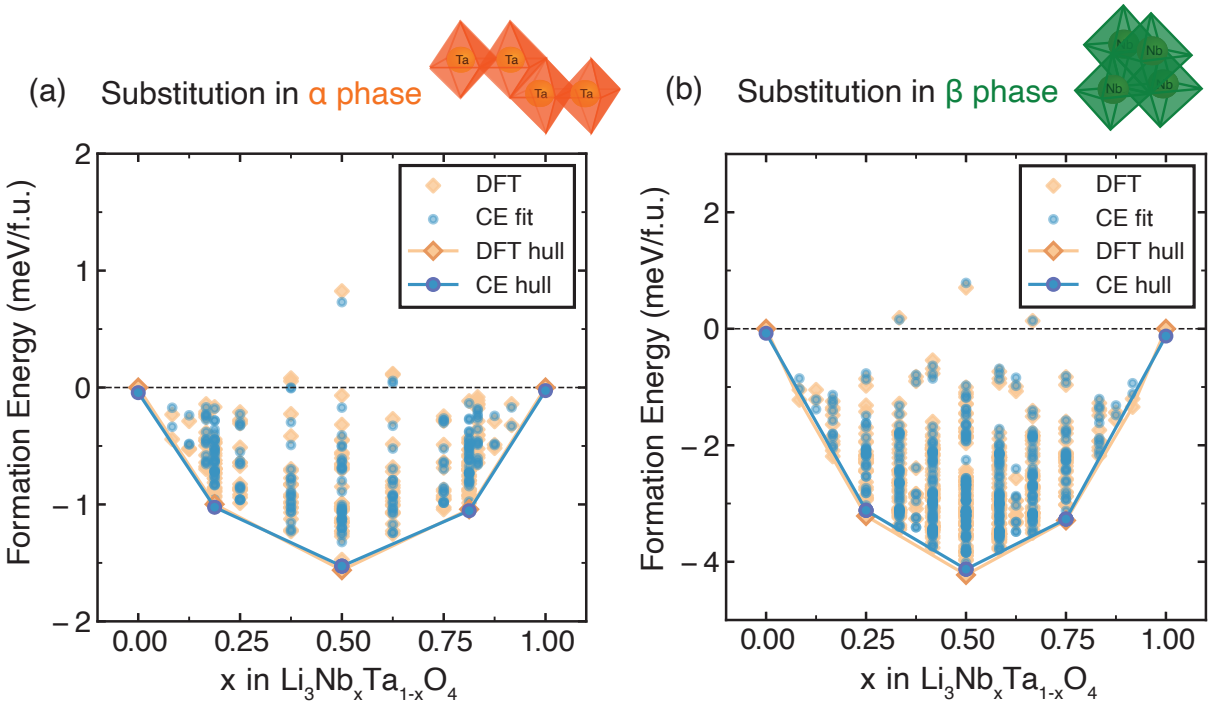

Figure S4: Configurational mixing energies, E_{mix}(conf), of Nb/Ta orderings vs. Nb concentration (x) in $Li_3Nb_xTa_{1-x}O_4$ starting from (a) α-phase ($C2/c$) Li_3TaO_4 and (b) β-phase ($I\bar{4}3m$) Li_3NbO_4. Orange diamonds represent orderings calculated by DFT, of which the most stable phases construct the convex hull shown as the solid line. The blue points and solid lines represent the mixing of energies from Nb/Ta orderings and convex hulls, as estimated by the cluster expansion model. Here, E_{mix}(conf) of β-phase-like Nb/Ta orderings applies β-phase Li_3NbO_4 and β-phase Li_3TaO_4 as end members, while E_{mix}(conf) of α-phase-like Nb/Ta orderings is referenced to α-phase Li_3NbO_4 and α-phase Li_3TaO_4. Note that the convex hull of the α phase consists of compositions at $x = 0$, 0.1875, 0.5, 0.8125, and 1.0. The orderings at $x = 0.1875$ and $x = 0.8125$ were constructed from 2×2×1 supercells, whereas the corresponding $x = 0.25$ and $x = 0.75$ orderings of 2×2×1 supercells were not included in the cluster expansion to avoid overfitting. The actual convex hull, when evaluated by DFT and cluster expansion using supercells of comparable sizes, is expected to occur at $x = 0$, 0.25, 0.5, 0.75, and 1.0, consistent with that of the β phase.

In the α-phase substitution (Figure S4a), the symmetrically inequivalent structures (221 of all supercells) computed with DFT are 1 for x=0 and x=1, 2 for x=0.083 and 0.917, 3 for x=0.125 and 0.875, 14 for x=0.167 and 0.833, 35 for x=0.1875 and 0.8125, 16 for x=0.25 and 0.75, 21 for x=0.375 and 0.625, 37 for x=0.5. In the β-phase substitution (Figure S4b), the symmetrically inequivalent structures (489 of all supercells) computed with DFT are 1 for

x=0 and x=1, 2 for x=0.083 and 0.917, 2 for x=0.125 and 0.875, 10 for x=0.167 and 0.833, 33 for x=0.25 and 0.75, 54 for x=0.33 and 0.67, 10 for x=0.375 and 0.625, 78 for x=0.417 and 0.583, 109 for x=0.5.

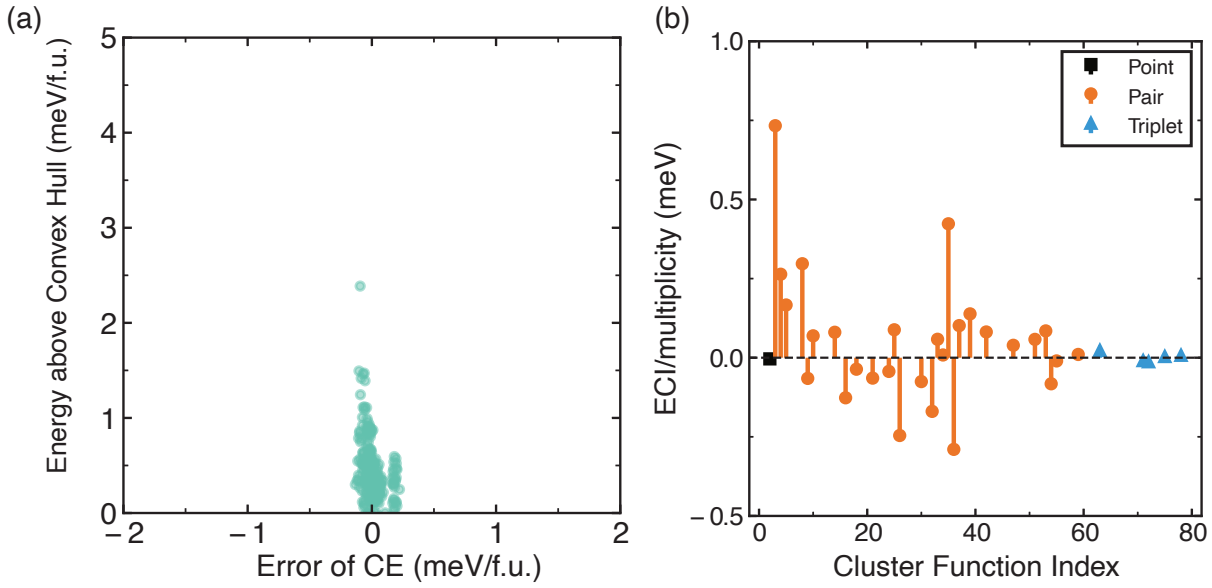

Figure S5: Error of cluster expansion fitting ($E_{\mathrm{CE}} - E_{\mathrm{DFT}}$), (b) ECIs of $Li_3Ta_{1-x}NbO_4$ in α-phase substitution. The RMS and LOOCV errors are 0.30 meV/f.u. and 0.36 meV/f.u., respectively.

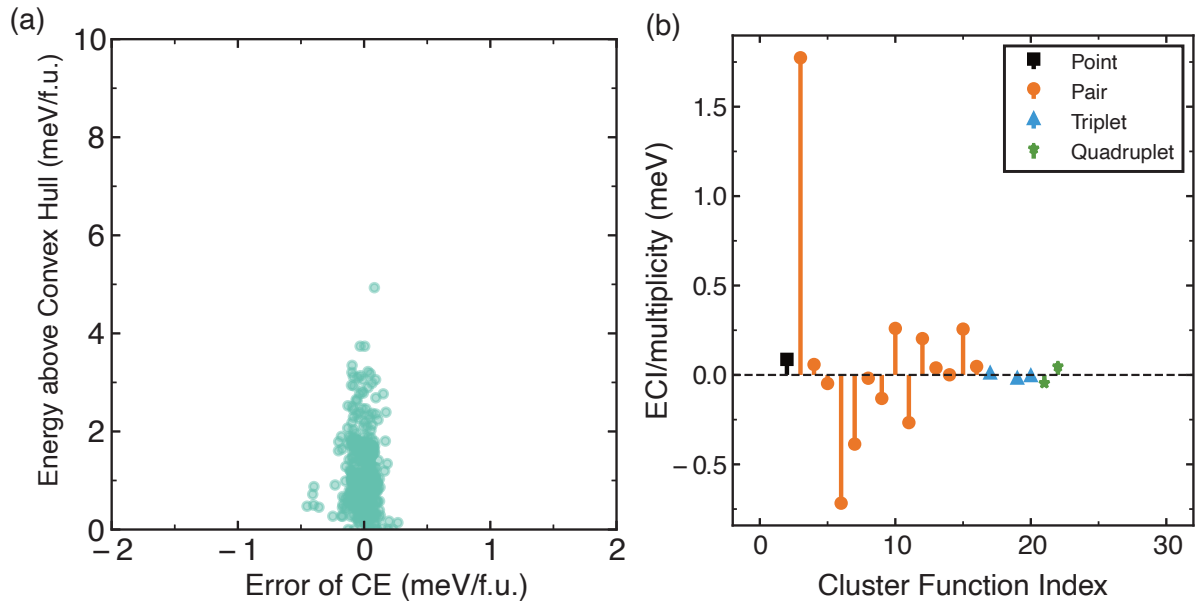

Figure S6: (a) Error of cluster expansion fitting ($E_{\mathrm{CE}} - E_{\mathrm{DFT}}$), (b) ECIs of $Li_3Ta_{1-x}NbO_3$ in β-phase substitution. The RMS and LOOCV errors are 0.33 meV/f.u. and 0.50 meV/f.u., respectively.

2 M-O Bond Lengths and Volume Changes of DFT-calculated Orderings

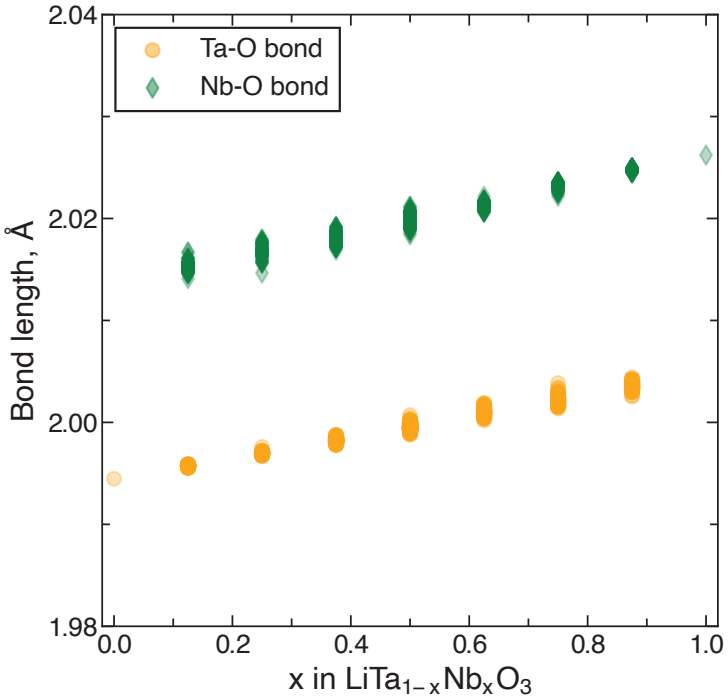

Figure S7: Distribution of average Ta-O and Nb-O bond lengths within DFT-calculated $LiNb_xTa_{1-x}O_3$ orderings at 0 K. A global trend that Ta-O bonds are always shorter than Nb-O bonds can be observed.

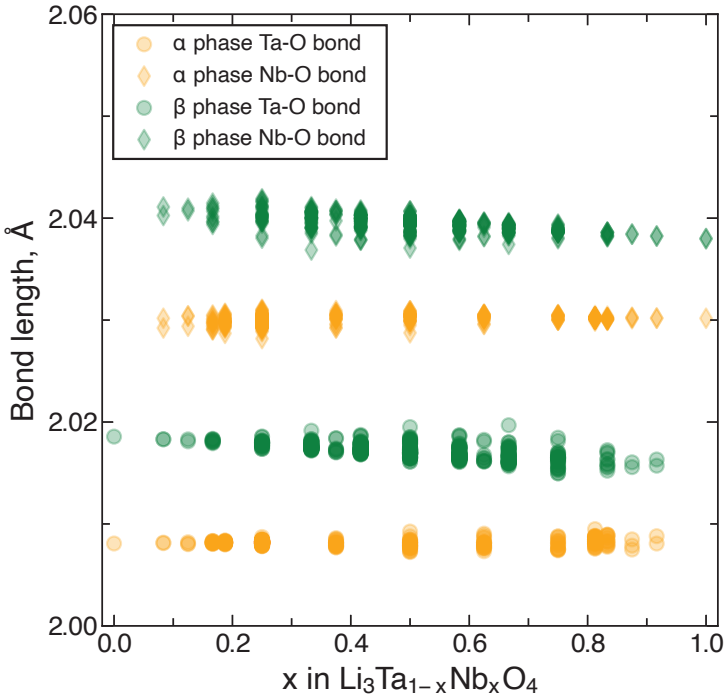

Figure S8: Distribution of average Ta-O (points) and Nb-O (diamonds) bond lengths within DFT-calculated $Li_3Nb_xTa_{1-x}O_4$ orderings templated on α-phase (orange) and β-phase (green) substitutions at 0 K.

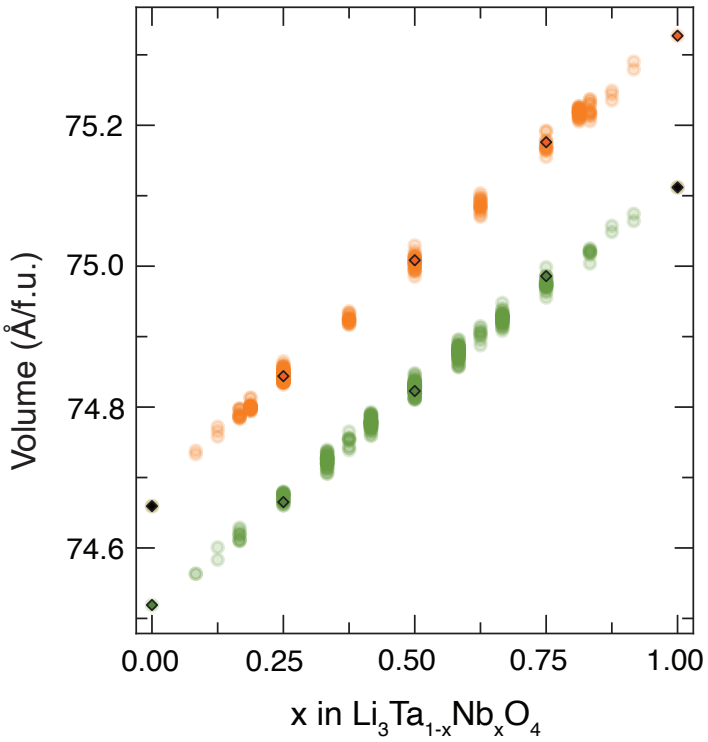

Figure S9: Distribution of cell volumes of all DFT-calculated $Li_3Nb_xTa_{1-x}O_4$ orderings templated on the α-phase (orange) and the β-phase (green) substitutions at 0 K.

3 Phonon Calculations for $Li_3Nb_xTa_{1-x}O_4$ ground-state structures

We utilized the Phonopy[S5] to evaluate phonons in the $Li_3Nb_xTa_{1-x}O_4$ via the finite displacement method. Phonons are used to estimate various thermodynamic figures using statistical thermodynamics, particularly the partition function, Z,

$$Z = exp(-\phi/k_BT)\prod_{\mathbf{q},j}\frac{\exp(-\hbar\omega_{\mathbf{q},j}/2k_BT)}{1-\exp(-\hbar\omega_{\mathbf{q},j}/k_BT)} \tag{1}$$

where k_B is the Boltzmann constant, q is the wave vector, j is the index of phonon mode, ω are vibrational eigenfrequencies, T is the temperature. The harmonic phonon energy E is calculated as:[S6]

$$E_{vib} = \sum_{\mathbf{q},j}\hbar\omega_{\mathbf{q},j}\left[\frac{1}{2}+\frac{1}{\exp(\hbar\omega_{\mathbf{q},j}/k_BT)-1}\right] \tag{2}$$

The Helmholtz vibrational free energy is calculated as,

$$F_{vib} = -k_BTlnZ = \frac{1}{2}\sum_{\mathbf{q},j}\hbar\omega_{\mathbf{q},j} + k_BT\sum_{\mathbf{q},j}\ln\left[1-\exp(-\hbar\omega_{\mathbf{q},j}/k_BT)\right] \tag{3}$$

Given $F = E - TS$, the vibrational entropy can be accessed via $S = -\frac{\partial F}{\partial T}$.

For each ground-state structure, the mixing vibrational energy is calculated as,

$$E_{mix}(\text{vib}) = E_{vib}(\text{Li}_3\text{Nb}_\text{x}\text{Ta}_{1-\text{x}}\text{O}_4) - xE_{vib}(\beta\text{-Li}_3\text{NbO}_4) - (1-x)E_{vib}(\alpha\text{-Li}_3\text{TaO}_4) \tag{4}$$

where E_{vib} are the harmonic phonon energies, α-phase Li_3TaO_4 ($C2/c$) and β-phase Li_3NbO_4 ($I\bar{4}3m$) are taken as references.

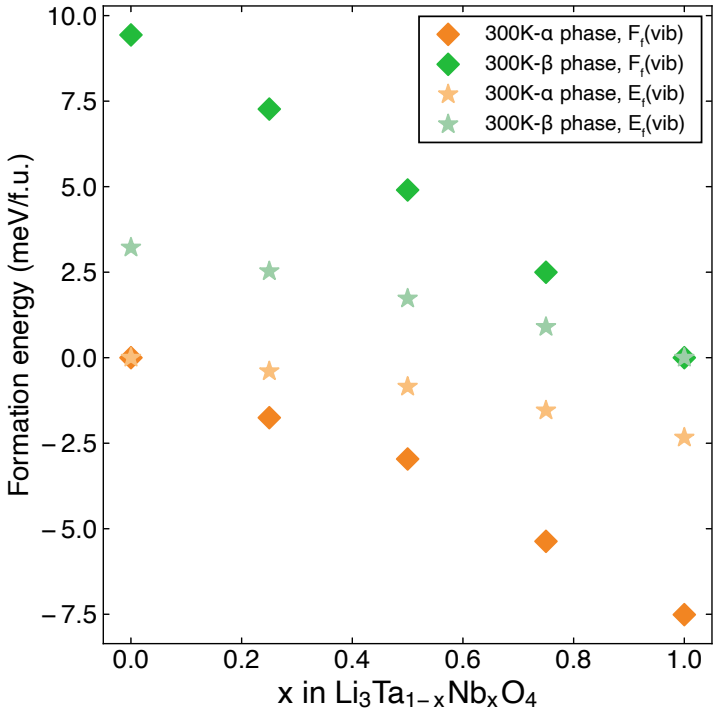

Figure S10: Mixing harmonic phonon energy, $E_{mix}(\text{vib})$, and mixing vibrational free energy, $F_{mix}(\text{vib}) = E_{mix}(\text{vib}) - TS_{mix}(\text{vib})$, of α and β phases ground-state structures are shown as a function of Nb concentration (x in $Li_3Nb_xTa_{1-x}O_4$) at 300 K. Given the nearly Vegard's law behavior, vibrational properties at other concentrations can be achieved through a smooth interpolation, as shown in Figure S11.

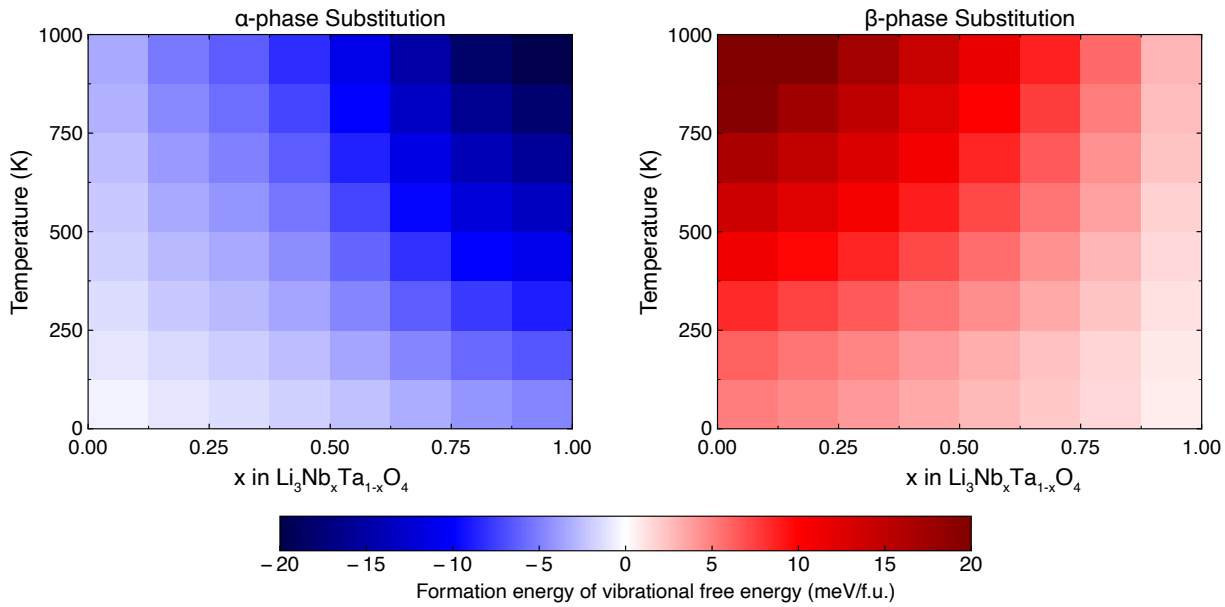

Figure S11: Mixing vibrational free energies, F_{mix}(vib), of Nb/Ta mixing orderings vs. x in $Li_3Nb_xTa_{1-x}O_4$ in (a) Nb-direction and (b) Ta-direction at different temperatures. The F_{mix}(vib) of ground-state structures (x=0.25, 0.5, 0.75, 1) are calculated by Phonopy, while F_{mix}(vib) of the other compositions are determined through cubic interpolation based on those of the ground-state structures.

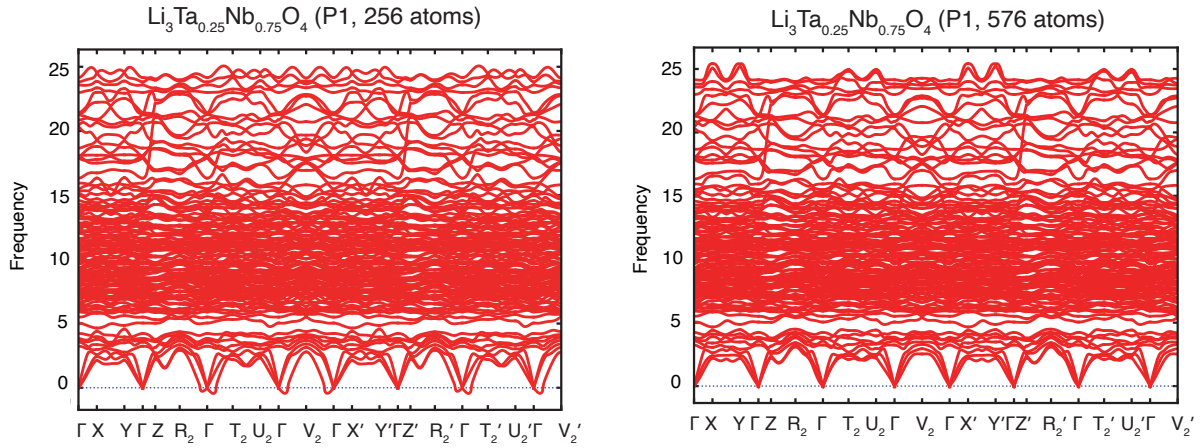

Figure S12: Convergence test on vibrational band structure calculations using (a) 2×2×2 supercell with some imaginary phonon modes (b) 3×3×2 supercell of α-phase $Li_{12}Ta_1Nb_3O_{16}$ ($Li_3Ta_{0.25}Nb_{0.75}O_4$) without any imaginary phonon modes. Frequencies are in THz. Imaginary phonon modes in (a) are due to numerical instabilities.

Table S1: Convergence test of vibrational free energies (F_{vib}) calculated using 2×2×2 supercell and 3×3×2 supercell of $Li_{12}Ta_1Nb_3O_{16}$ with displacements. The minimal negative phonons in the 2×2×2 supercell model are attributed to numerical issues. While the band structure of a 2×2×2 supercell may not eliminate all imaginary modes, the vibrational properties, i.e., harmonic phonon energies, E_{vib}, and vibrational free energies, F_{vib}, exhibit minimal deviations compared to those obtained from larger supercells (3×3×2). As a result, we applied 2×2×2 supercells for the vibration calculations of other structures to mitigate computational costs.

	2×2×2 $Li_{12}Ta_1Nb_3O_{16}$ (eV/f.u.)	3×3×2 $Li_{12}Ta_1Nb_3O_{16}$ (eV/f.u.)	deviation
0 K - $E_{vib} = F_{vib}$	0.5436	0.5443	-0.124 %
1000 K - E_{vib}	2.0542	2.0549	-0.033 %
1000 K - F_{vib}	-1.4219	-1.4185	0.239 %

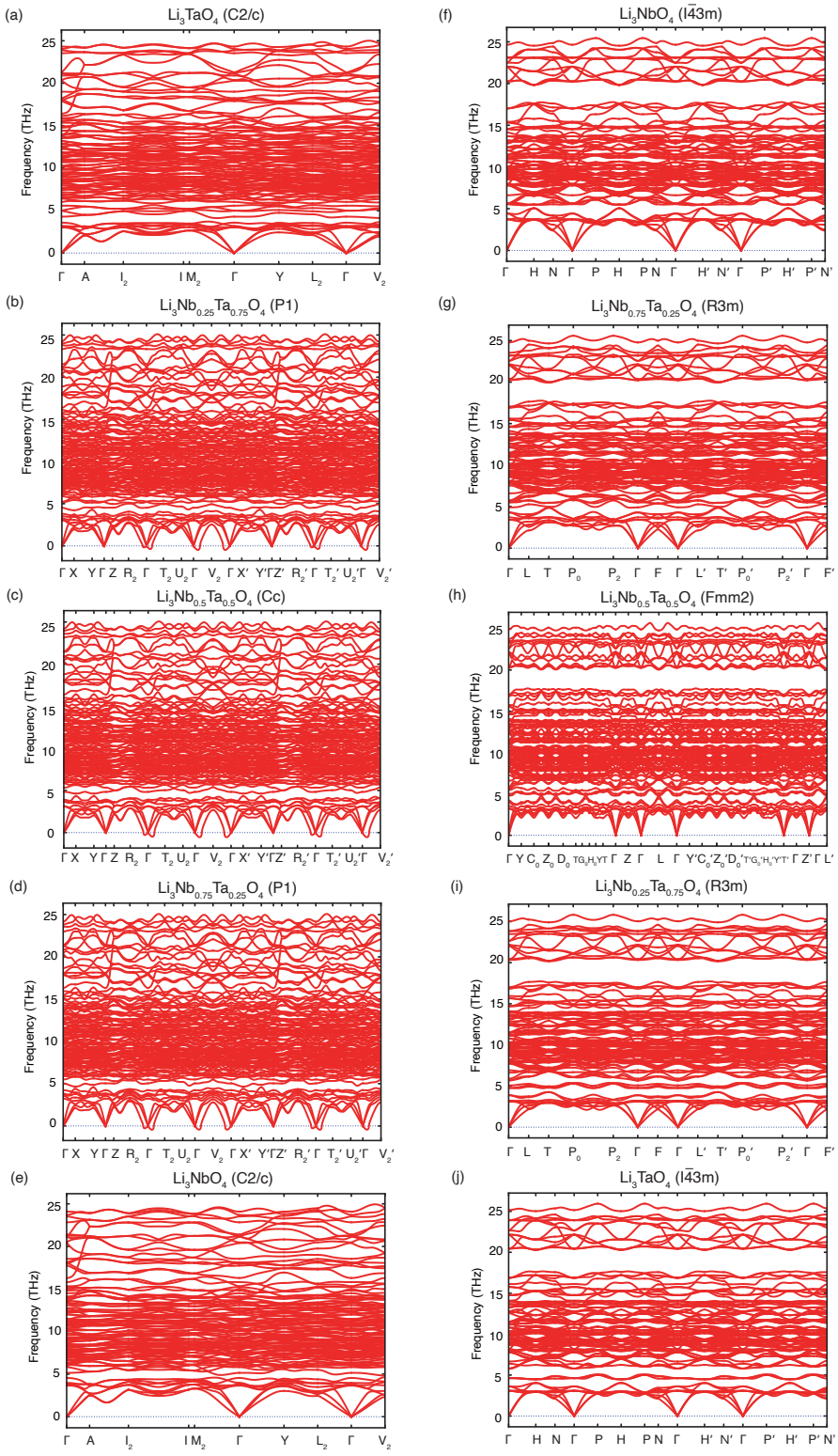

Figure S13: Vibrational band structures of all DFT-calculated (a)-(e) α-phase and (f)-(j) β-phase ground-state structures.

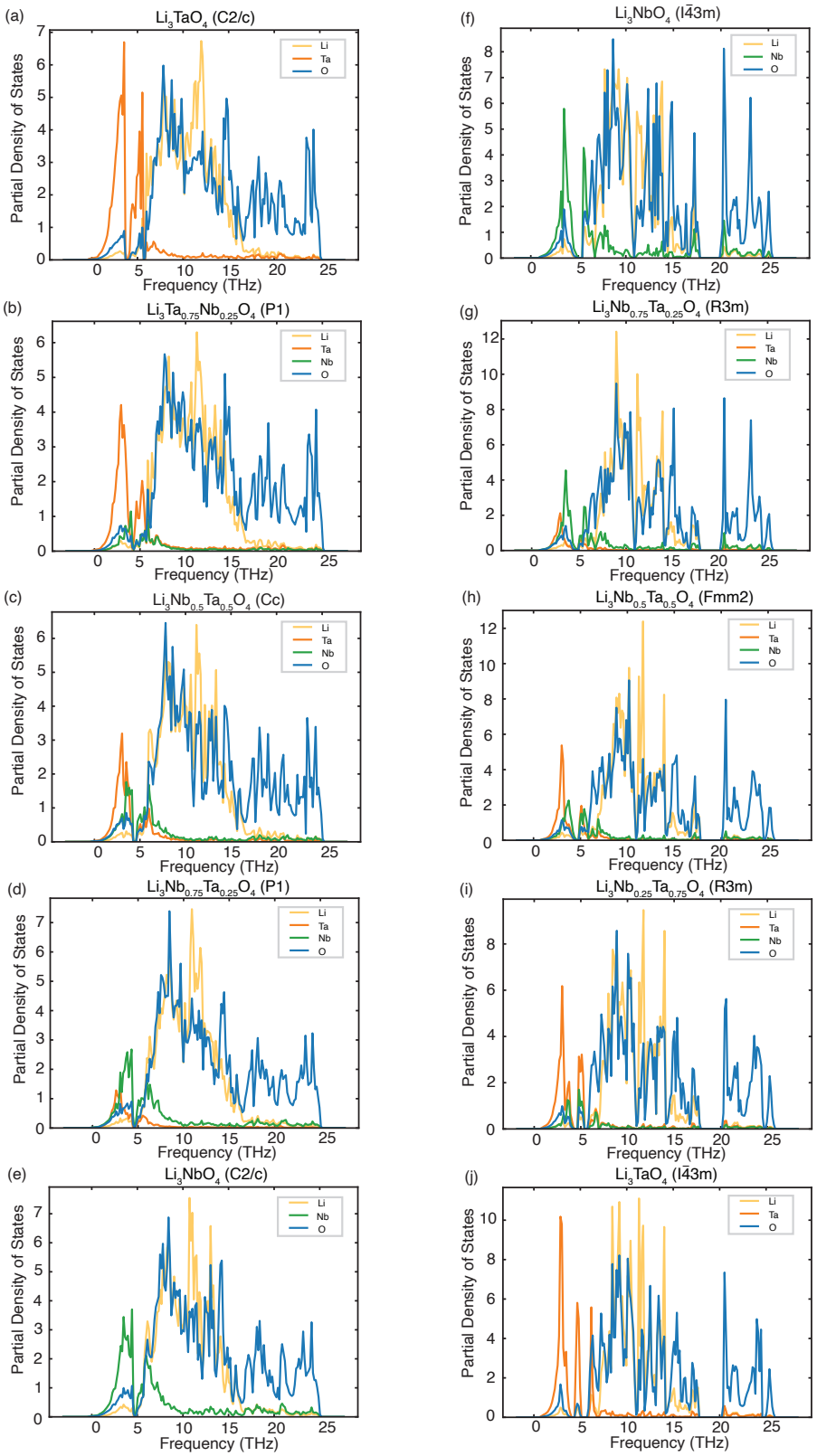

Figure S14: Phonon density of states of (a)-(e) α-phase, and (f)-(j) β-phase ground-state structures.

4 Computed phase diagram of $LiNb_xTa_{1-x}O_3$

Combining cluster-expansion and semi-grand canoncial Monte Carlo simulations, our computed phase diagram (Figure S15) illustrates that a $LiNb_xTa_{1-x}O_3$ solid solution can form across the entire compositional range, which is consistent with experimental observations.[S4,S7]

To further refine this picture, we also investigated the influence of vibrational free energy. Given the lack of true ground-state structures for the $LiNb_xTa_{1-x}O_3$ system, we selected representative orderings with the lowest mixing configurational energies for the phonon calculations (Figure S1b). The relationship between Phonopy-calculated vibrational free energies and Nb composition is plotted in (Figure S16). While the calculated mixing vibrational free energies are negative, known to stabilize disordered states relative to the ordered states and reducing the transition temperature,[S8,S9] this stabilizing contribution is very small. It only lowers the miscibility gap marginally without altering the overall shape of the phase diagram (Figure S15). This indicates that vibrational effects do not play a decisive role in this system.

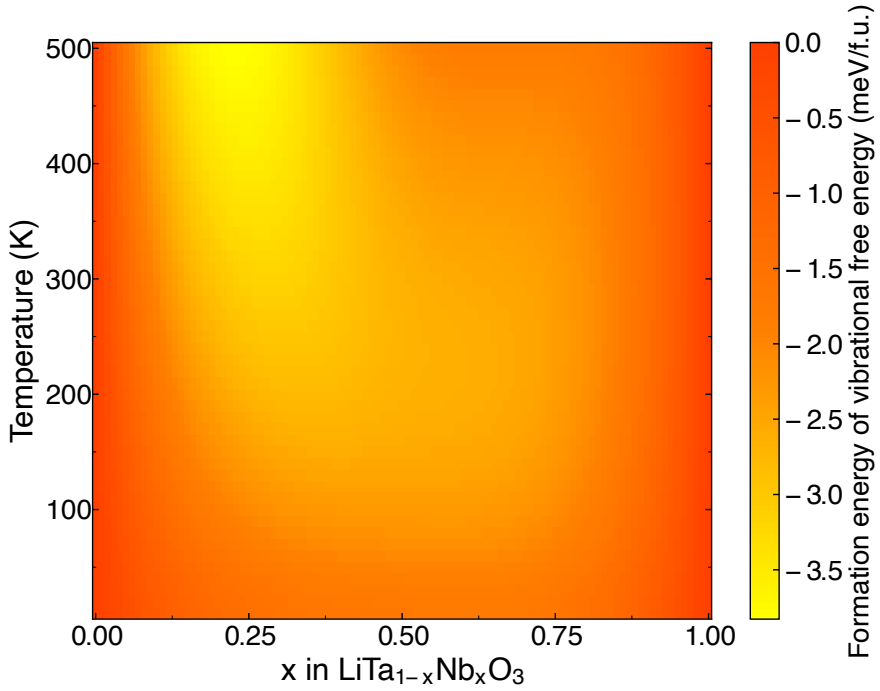

Figure S15: Mixing vibrational free energies, F_{mix}(vib), of metastable configurations with lowest DFT-energies at x=0.25, 0.5, 0.75, referenced to stable end points, *i.e.*, $LiTaO_3$ and $LiNbO_3$.

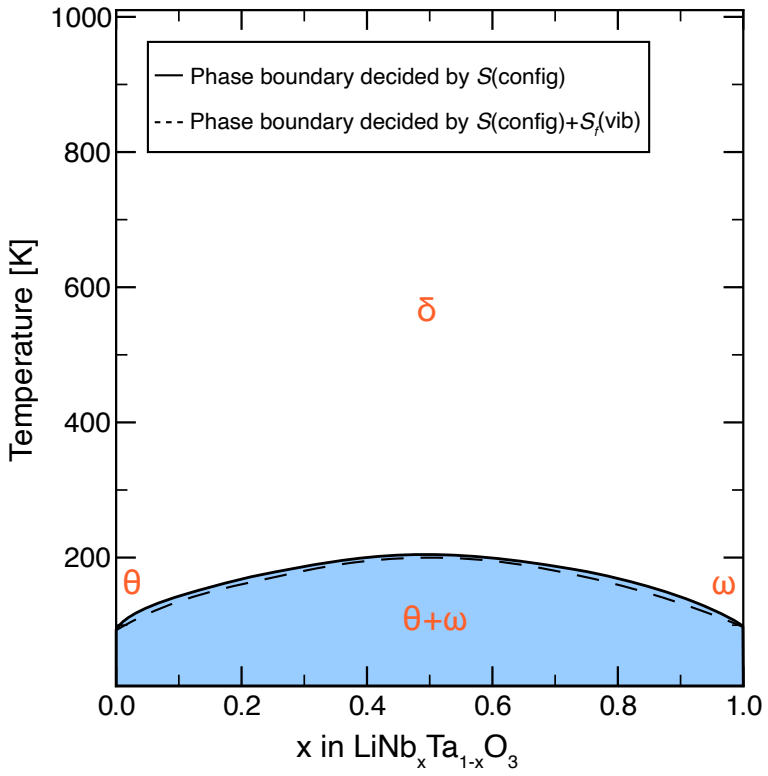

Figure S16: Computed phase diagrams of $LiNb_xTa_{1-x}O_3$ from semi-grand canonical Monte Carlo (semi-gcMC) simulations, where configurational contributions give the solid line of the phase boundary, and the slightly lower dashed line represents the phase boundary after adding the vibrational contributions.

5 Thermodynamic Integration

When considering both configurational and vibrational contributions in the semi-grand canonical Monte Carlo (semi-gcMC), the grand-potential Φ (per prim cell here, 4 f.u. here) associated with the grand-canonical ensemble (μVT) can be defined in terms of the partition function, Z, of the system as follows:[S10]

$$\Phi(\mu,\beta) = -\frac{1}{\beta}\ln Z = -\frac{1}{\beta}\ln\sum_{\sigma}\exp(-\beta\underbrace{(E_{mix}(\text{conf}) + F_{mix}(\text{vib}) - \mu x)}_{\text{potential energy (PE)}}) \tag{5}$$

where $\beta = \frac{1}{k_B T}$, E_{mix}(conf) is the cluster-expanded mixing energy dependent on specific configurations, F_{mix}(vib) is the mixing vibrational free energy, x denotes the Nb concentration. In semi-gcMC simulations, the difference in potential energies (dPE = dE_{mix}(config) + dF_{mix}(vib) − μdx) between MC swaps is used to determine the $\mu - x$ relationship, i.e., whether to accept a new MC event or not.

We have determined the composition phase diagram using two methods:

(1) Include dF_{mix}(vib) into dPE and F_{mix}(vib) into PE. Therefore, the total differential of Φ can be defined as,

$$d\beta\Phi(\mu,\beta) = (E_{mix}(\text{conf}) + F_{mix}(\text{vib}) - \mu x)d\beta - \beta x d\mu \tag{6}$$

When μ is fixed (for each $\mu \in [-1,1], \Delta\mu = 0.01$), from low to high temperature (T increases from 10 K to 1000 K with a step $\Delta T = 10K$), we integrate the configurational and vibrational sections,

$$\beta_1\Phi(\mu,\beta_1) = \beta_0\Phi(\mu,\beta_0) + \int_{\beta_0}^{\beta_1}(E_{mix}(\text{conf}) + F_{mix}(\text{vib}) - \mu x)d\beta,\ \mu\,\text{fixed} \tag{7}$$

When T is fixed (for each $T \in [10,1000]K, \Delta T = 10K$), gcMC simulations scan from low to

high (or inverse) μ (from -1 to 1 with $\Delta\mu = 0.01$, or from 1 to -1 with $\Delta\mu = -0.01$),

$$\beta\Phi(\mu_1, \beta) = \beta\Phi(\mu_0, \beta) - \beta \int_{\mu_0}^{\mu_1} x d\mu, \text{ T fixed} \tag{8}$$

In this case, for a α-phase, the total thermodynamic potential energy, Φ_{tot}, can be decomposed as:[S8]

$$\Phi_{tot} = \Phi_{\text{semi-gcMC}} = F - \mu x = E^{\alpha}_{mix}(\text{conf}) + F^{\alpha}_{mix}(\text{vib}) - TS^{\alpha}(\text{conf}) - \mu x \tag{9}$$

where the configurational entropy, $S^{\alpha}(\text{conf})$, can be achieved through the integration. However, $F_{mix}(\text{vib})$ is not solely a function of composition but also exhibits a significant temperature dependence (Eq. 3). This means Eq. 6 should include a derivative term, such as, $\frac{\partial F_{mix}(\text{vib})}{\partial \beta}\beta d\beta$. But this differential and subsequent integration, $\int_{\beta_0}^{\beta_1} \frac{\partial F_{mix}(\text{vib})}{\partial \beta}\beta d\beta$, in Eq. 5, may double-counting or mis-weighting entropy contributions.

(2) Therefore, we only include $dF_{mix}(\text{vib})$ in the definition of dPE, but exclude $F_{mix}(\text{vib})$ from the PE, treating the configurational and vibrational integration sections separately. For a phase α, the total grand canonical free energy Φ_{tot} is given as,

$$\Phi_{tot} = \Phi_{\text{semi-gcMC}} + F^{\alpha}_{mix}(\text{vib}) \tag{10}$$

where $F_{mix}(\text{vib})$ is added to $\Phi_{\text{semi-gcMC}}$ according to the $(\mu \leftrightarrow x, T)$ grid.

When μ is fixed, T changes,

$$\beta_1\Phi(\mu, \beta_1) = \beta_0\Phi(\mu, \beta_0) + \int_{\beta_0}^{\beta_1} (E_{mix}(\text{conf}) - \mu x) d\beta, \ \mu \text{ fixed} \tag{11}$$

Here $\Phi_{tot}(\mu, \beta_1) = \Phi(\mu, \beta_1) + F_{mix}(\text{vib})(\mu, \beta_1)$. When T is fixed, μ changes,

$$\beta\Phi(\mu_1, \beta) = \beta\Phi(\mu_0, \beta) - \beta \int_{\mu_0}^{\mu_1} x d\mu, \text{ T fixed} \tag{12}$$

where $\Phi(\mu_0, \beta)$ is taken from Φ_{tot}, including $F_{mix}(\text{vib})(\mu, \beta_0)$ contribution. In the harmonic approximation, the vibrational energy $E(\text{vib})$ (determined by the equipartition theorem) and the vibrational entropy $S(\text{vib})$ (determined by $-\frac{\partial F}{\partial T}$) influence the phase stability through the vibrational free energy, $F(\text{vib}) = E(\text{vib}) - TS(\text{vib})$. Therefore, the corresponding mixing energies can be represented as $F_{mix}(\text{vib}) = E_{mix}(\text{vib}) - TS_{\text{mix}}(\text{vib})$. Here, $S_{\text{mix}}(\text{vib})$ is the vibrational entropy of mixing, calculated as the difference in vibrational entropy between $Li_3Nb_xTa_{1-x}O_4$ orderings and the pristine compounds α-Li_3TaO_4 and β-Li_3NbO_4.[S11,S12]

For a phase α, the total thermodynamic grand potential energy, Φ_{tot}, can be decomposed as:[S8]

$$\Phi_{tot} = E^{\alpha}_{mix}(\text{conf}) - TS^{\alpha}(\text{conf}) - \mu x + E^{\alpha}_{mix}(\text{vib}) - TS^{\alpha}_{\text{mix}}(\text{vib}) \tag{13}$$

The vibrational contributions are then inserted into the CASM code (see `https://github.com/caneparesearch/CASMcode/tree/hengning_Fvib`), where we incorporated $dF_{mix}(\text{vib})$ into the event decision process to determine the $\mu - x$ relationship. The complete phase diagram was obtained by minimizing the semi-grand canonical potential by comparing Φ at specific compositions of the two phases.

$$\Phi_{\text{semi-gcMC}} = min\langle \Phi_{\alpha,\text{forward}}, \Phi_{\alpha,\text{backward}}, \Phi_{\beta,\text{forward}}, \Phi_{\beta,\text{backward}} \rangle \tag{14}$$

6 Li-ion conductivities of $Li_3Nb_xTa_{1-x}O_4$ from MTP-MD simulations

System	Training MAE	
	Energy (meV/atom)	Force (eV/Å)
α-Li_3TaO_4	3.86	0.58
α-$Li_3Nb_{0.125}Ta_{0.875}O_4$	4.33	0.59
α-$Li_3Nb_{0.1875}Ta_{0.8125}O_4$	3.99	0.59
β-$Li_3Nb_{0.6875}Ta_{0.3125}O_4$	3.55	0.60
β-$Li_3Nb_{0.75}Ta_{0.25}O_4$	3.37	0.60
β-Li_3NbO_4	3.33	0.60

Figure S17: Mean Absolute Errors (MAE) for energies (meV/atom) and forces (eV/$\AA$) of the Moment Tensor Potential. The training set consists of 32000 configurations extracted from the final 4 ps (8000 configurations) of AIMD simulations at each temperature (600, 800, 1000, and 1200 K), with 4000 configurations split for the validation set

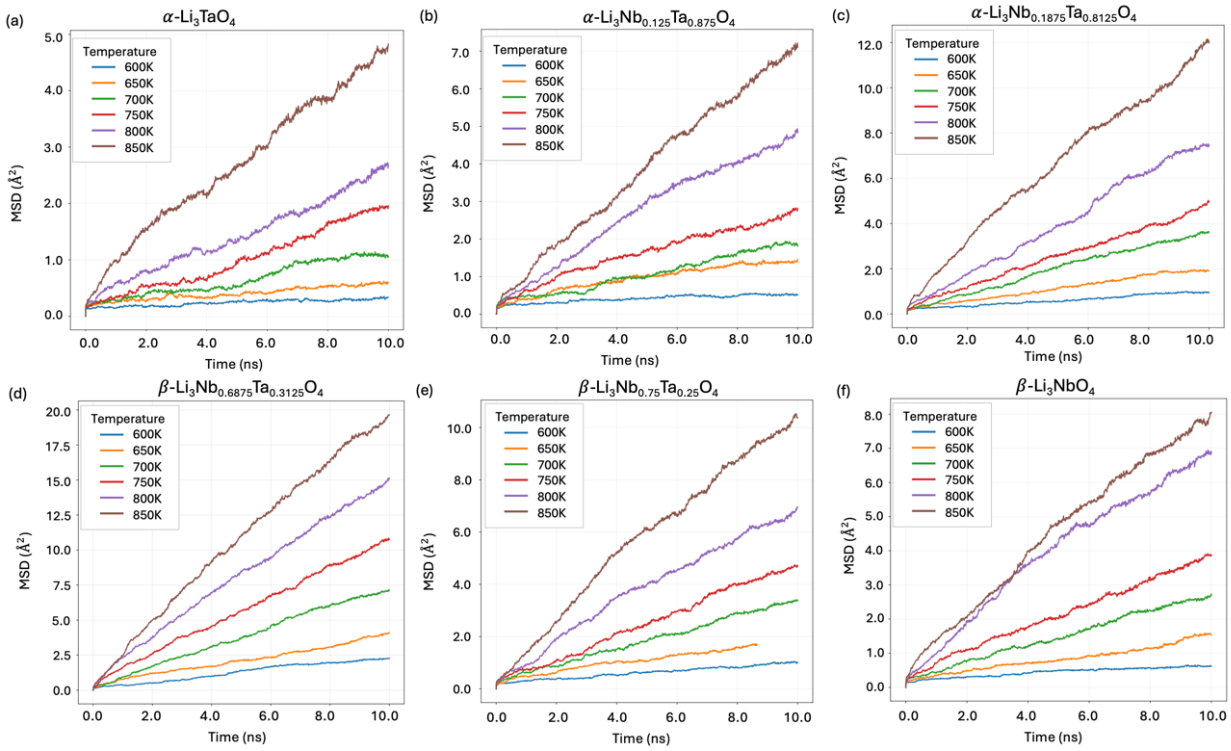

Figure S18: MTP-MD calculated mean square displacements (MSD) of Li ions in $Li_3Nb_xTa_{1-x}O_4$ configurations (a) $x = 0$, (b) $x = 0.125$, (c) $x = 0.1875$, (d) $x = 0.6875$, (e) $x = 0.75$, (f) $x = 1$ at temperatures ranging from 600 K to 850 K. The subsequent Li-ion conductivities were calculated from the slope of a linear fit to the MSD data over time.

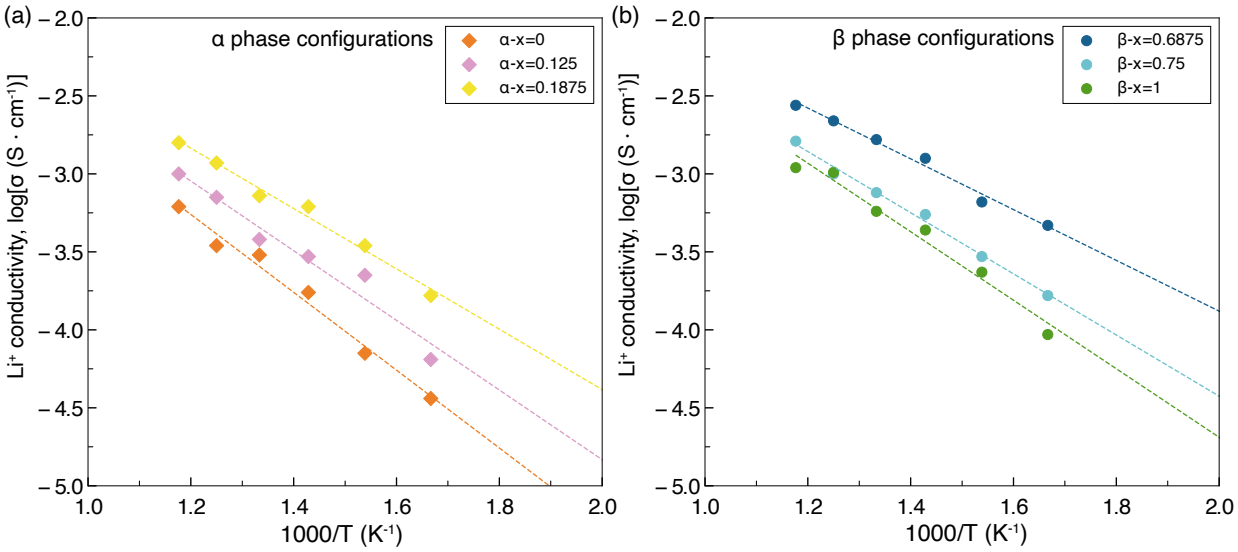

Figure S19: Arrhenius plots of MTP-MD calculated Li-ion conductivities in the (a) α-phases and (b) β-phases of $Li_3Nb_xTa_{1-x}O_4$ over a temperature range of 600-850 K. The structural configurations were obtained from semi-grand canonical Monte Carlo simulations.

References

(S1) Kresse, G.; Furthmüller, J. Efficient iterative schemes forab initiototal-energy calculations using a plane-wave basis set. *Phys. Rev. B* **1996**, *54*, 11169–11186.

(S2) Kresse, G.; Joubert, D. From ultrasoft pseudopotentials to the projector augmented-wave method. *Physical Review B* **1999**, *59*, 1758–1775.

(S3) Furness, J. W.; Kaplan, A. D.; Ning, J.; Perdew, J. P.; Sun, J. Accurate and Numerically Efficient r2SCAN Meta-Generalized Gradient Approximation. *The Journal of Physical Chemistry Letters* **2020**, *11*, 8208–8215.

(S4) Huband, S.; Keeble, D. S.; Zhang, N.; Glazer, A. M.; Bartasyte, A.; Thomas, P. A. Crystallographic and optical study of $LiNb_{1-x}Ta_xO_3$. *Acta Crystallographica Section B Structural Science, Crystal Engineering and Materials* **2017**, *73*, 498–506.

(S5) Togo, A.; Tanaka, I. First principles phonon calculations in materials science. *Scripta Mater.* **2015**, *108*, 1–5.

(S6) Togo, A. First-principles Phonon Calculations with Phonopy and Phono3py. *J. Phys. Soc. Jpn.* **2023**, *92*, 012001.

(S7) Bartasyte, A.; Glazer, A.; Wondre, F.; Prabhakaran, D.; Thomas, P.; Huband, S.; Keeble, D.; Margueron, S. Growth of $LiNb_{1-x}Ta_xO_3$ solid solution crystals. *Mater. Chem. Phys.* **2012**, *134*, 728–735.

(S8) van de Walle, A.; Ceder, G. The effect of lattice vibrations on substitutional alloy thermodynamics. *Rev. Mod. Phys.* **2002**, *74*, 11–45.

(S9) Ozoliņš, V.; Wolverton, C.; Zunger, A. First-principles theory of vibrational effects on the phase stability of Cu-Au compounds and alloys. *Physical Review B* **1998**, *58*, R5897–R5900.

(S10) van de Walle, A.; Asta, M. Self-driven lattice-model Monte Carlo simulations of alloy thermodynamic properties and phase diagrams. *Model. Simul. Mater. Sc.* **2002**, *10*, 521–538.

(S11) Delaire, O.; Swan-Wood, T.; Fultz, B. Negative Entropy of Mixing for Vanadium-Platinum Solutions. *Phys. Rev. Lett.* **2004**, *93*, 185704.

(S12) Gao, M. C.; Gao, P.; Hawk, J. A.; Ouyang, L.; Alman, D. E.; Widom, M. Computational modeling of high-entropy alloys: Structures, thermodynamics and elasticity. *J. Mater. Res.* **2017**, *32*, 3627–3641.